ANNUAL AND INTERANNUAL VARIATIONS OF EARTH-EMITTED RADIATION BASED ON A 10-YEAR DATA SET

by

T. DALE BESS, G. LOUIS SMITH, AND THOMAS P. CHARLOCK
ATMOSPHERIC SCIENCES DIVISION
NASA LANGLEY RESEARCH CENTER
HAMPTON, VIRGINIA 23665-5225

and

FRED G. ROSE

PLANNING RESEARCH CORPORATION
HAMPTON, VIRGINIA 23666

Submitted to

JOURNAL OF CLIMATE

January 1989

ANNUAL AND INTERANNUAL VARIATIONS OF EARTH-EMITTED RADIATION BASED ON A 10-YEAR DATA SET

T. Dale Bess[1], G. Louis Smith[1], Thomas P. Charlock[1], and Fred G. Rose[2]

Abstract

The method of empirical orthogonal functions (EOF) has been applied to a 10-year data set of outgoing longwave radiation. Spherical harmonic functions are used as a basis set for producing equal area map results. The following findings are noted. The first EOF accounts for 66% of the variance. After that, each EOF accounts for only a small variance, forming a slowly converging series. The first two EOF's describe mainly the annual cycle. The third EOF is primarily the semi-annual cycle although many other EOF's also contain significant semi-annual parts. These results reaffirm those based on a shorter data set.

In addition, a much stronger spring/fall mode was found in the central equatorial Pacific Ocean for the second EOF than was found earlier. This difference is attributed to the use of broadband radiometer data which were available for the present study. The earlier study used data from a window channel instrument which is not as sensitive to water vapor variations. The fourth EOF describes much of the 1976-77 and 1982-83 ENSO phenomena. There is typically a gap in the spectrum between a semiannual peak and the annual cycle for all but the first EOF. A semiannual OLR dipole straddles the Asian-Australian monsoon track.

1 Atmospheric Sciences Division, NASA Langley Research Center, Hampton, Virginia, 23665-5225

2 Planning Research Corporation, Hampton, Virginia 23666

1. Introduction

Outgoing longwave radiation (OLR) is one of the primary quantities which govern our weather and climate; thus it has been the subject of a great deal of research. An understanding of the space and time variations of OLR is necessary to the understanding of climate and its fluctuations at all scales. The studies of OLR prior to the advent of satellites are reviewed by Hunt et al. (1986). Because satellites are so well suited to the measurement of OLR, they have been used for this purpose since very early in the development of spacecraft (House et al., 1986).

Winston et al. (1979) used the Scanning Radiometer (SR) aboard operational meteorological satellites to compute OLR and published a 44-month data set for the period June 1974 through March 1978. The SR has a window channel for monitoring sea-surface temperature and for providing cloud imagery, so it is necessary to infer broadband OLR from narrow band (window) measurements by using a narrowband to broadband conversion algorithm. Nevertheless, the availability of this data set has made it immensely useful for Earth radiation budget studies. Heddinghaus and Krueger (1981) studied these 44 months using an empirical orthogonal function (EOF) approach and obtained many interesting results.

The EOF approach has been used by other investigators for studying other meteorological variables, such as sea level pressure and surface temperature (Kutzbach, 1967), teleconnection patterns (Horel and Wallace, 1981; Wallace and Gutzler, 1981), and temporal variability (Holmstrom, 1970)

At the time of the study by Heddinghaus and Krueger (1981), the only long-term data radiation data set was that developed by Winston et al. (1979), which used data from the scanning radiometer SR on the NOAA operational spacecraft. Because the SR is a window-channel instrument, it is relatively insensitive to OLR variations due to changes in water vapor or atmospheric temperature; the most important water vapor and carbon dioxide bands are outside the window. Nevertheless, a large number of important findings have been based on that data set, e.g., Lau and Chan (1986).

In order to obtain broadband measurements of the OLR and solar radiation reflected by the Earth, an Earth Radiation Budget (ERB) instrument was flown on the Nimbus-6 spacecraft in June 1975 (W. L. Smith et al., 1977) and another on the Nimbus-7 spacecraft in October 1978 (Jacobowitz et al., 1984). The wide field-of-view (WFOV) radiometers on these spacecraft are broadband instruments which measure OLR over all wavelengths at which significant thermal radiation occurs. They have provided a nearly continuous record of data from July 1975 to the present. Bess and Smith (1987a and b) have computed resolution enhanced monthly average OLR using the deconvolution method of G. L. Smith and Green (1981) and compiled them in readily usable form for monthly averages over the 10-year period July 1975 through October 1985. This data set is expressed as spherical harmonic coefficients through degree 12 and, as such, is very compact. Basically, this data set is well-suited for studies of annual and interannual variations for spatial scales of 15^{o} of geocentric arc distance and greater.

The purpose of the present paper is to examine the 10-year data set of Bess and Smith (1987a and b) for the period 1975 through 1985 using the empirical orthogonal function technique as done by Heddinghaus and Krueger (1981). The major reason for following this approach is that the data record now extends to a full decade, whereas Heddinghaus and Krueger (1981) had less than 4 years of data with which to work. The additional period of data includes the 1982-83 El Niño/ southern oscillation (ENSO) event which is the strongest ever observed with good coverage of instrumentation. Also, the present study will use data from a broadband radiometer rather than from a window-channel radiometer. A fundamental question for any study such as the present one is how representative is the time period being investigated?

2. Analysis method

The OLR data sets of Bess and Smith (1987a and b) consist of tables which describe monthly mean OLR fields. There are 120 months of data covering the period July 1975 through June 1978 and November 1978 through 1985. There is a 4-month gap between Nimbus-6 and Nimbus-7 measurements.

In applying the method of empirical orthogonal functions EOF's to global fields of OLR, it is intrinsically assumed that the monthly radiation fields are realizations of a random vector. Usually this vector is the value of the OLR field at the grid points in the map, so that it represents a field which is randomly distributed in space. The EOF analysis provides a method for studying the statistical characteristics of the spatial and temporal structure.

The vector $\underline{y}$ is defined as the array of OLR grid-point values, such that the OLR at grid point p is the p-th component of the vector. The dimensionality of the vector is the number of grid points, P. For the present case, there are 120 months of data, so that I = 120 realizations. The mean $\langle \underline{y} \rangle$ of the data set is first computed for each of the 12 calendar months, and then the deviation $\underline{x}_i = \underline{y}_i - \langle \underline{y} \rangle$ is computed for each month i (i = 1,120). The covariance matrix can be computed as

$$C = \sum_{i=1}^{I} \underline{x}_i \underline{x}_i^t / I \qquad (1)$$

The eigenvalues λ_k and eigenvectors $\underline{u}_k$ of the C matrix can then be computed:

$$C\,\underline{u}_k = \lambda_k \underline{u}_k \qquad (2)$$

The covariance matrix is real and symmetric, thus its eigenvalues λ_k are real, and its eigenvectors are real and orthogonal. The eigenvectors $\underline{u}_k$ thus form a basis set for the representation of the OLR fields:

$$\underline{x}_i = \sum_{k=1}^{K} \alpha_{ik} \underline{u}_k \qquad (3)$$

These α_{ik} coefficients can be computed by the orthogonality property of the $\underline{u}_k$:

$$\alpha_{ik} = \underline{x}_i^t \, \underline{u}_k \qquad (4)$$

Also, the α_{ik} are orthogonal to each other, which implies that they are uncorrelated with each other for zero lag. It can be shown that the EOF's are the most economical basis for expressing the fields in the sense that for a given number of coefficients, more of the variance can be accounted for by this expansion than by any other. Thus, in order to study the time variation of a spatially varying field, the α_{ik} form the set which will be the smallest for a given level of accuracy in its description. Furthermore,

$$\sum_{i=1}^{I} (\alpha_{ik})^2 / I = \lambda_k \qquad (5)$$

that is, the variance explained by the k-th coefficients in the series is the k-th eigenvalue. The EOF expansion of eq. (3) may be thought of as analogous to a Fourier series or modal expansion, except that the vectors are defined by the data set itself.

For the present case, the OLR fields are described by Bess and Smith (1987a and b) in terms of spherical harmonic coefficients through degree and order 12. One approach to the EOF computation is to compute the

grid point values and then compute the EOF's in terms of grid points. Another approach is to compute the EOF's in terms of the spherical harmonic coefficients and then to map them into grid points. For a spherical harmonic expansion through 12th degree and order, the $\underline{x}_i$ have a dimensionality of 169 and their covariance matrix S will be 169x169. A 10°x10° grid will require 648 grid points for global coverage. It is thus quite advantageous to use the spherical harmonic coefficients as a basis for the computations, and then to transform the results into the grid system. The question arises, Do we get the same results from both methods? The answer is that the results are the same if, and only if, we use a grid system of equal area boxes (to the level of accuracy of the mapping between the spherical harmonic coefficients and the grid system). However, the results are different if a latitude-longitude grid is used, as this system will weight the regions near the poles far more heavily than will an equal area grid system. Furthermore, in that case, the EOF's of the two systems will not be simply related. Any EOF computations for global coverage should be based on an equal area grid in order to have physical significance. The equivalence of such EOF's to EOF's computed on a spherical harmonic basis is demonstrated in the appendix. Because of its economy, the computations in this paper were done on the spherical harmonic basis.

3. Results and discussion

Empirical orthogonal functions were computed using the spherical harmonic coefficients and then transforming them into a latitude-longitude map. The percentages of variance associated with each eigenvector and the cumulative percentages of variance are listed in Table 1 for the first 10 EOF's. These variances are very near the results of Heddinghaus and Krueger (1981) for which they list the first five. It is noted that they used a latitude-longitude grid from 60°S to 60°N for their investigations. In this manner, they avoided the regions further poleward, where the equal area consideration would become a major problem. Also, for the bands between 50° and 60° in each hemisphere, they reduced the longitudinal spacing from 20° used in the rest of the domain to 40° in order to reduce the inequality of the grid areas. In the present work the first 10 terms account for 85% of the variance, and the 10th term is less than 1%. The convergence of the eigenvalues beyond these first 10 is quite slow. Inclusion of the first 40 terms gives 96% of the variance, an increase due to terms 11 through 40 of 11%, and the 40th term contains 0.17% of the variance.

The eigenvalues are seen in Table 1 to become closely spaced as rank increases. The significance of these numbers (which are statistical and thus random in their nature) must be examined. The criterion of North et al. (1982) for noise level in the eigenvalues is $\lambda_k(2/N)^{1/2}$, where N is the number of independent realizations. This quantity is also listed in the table, with a value of N = 60 assumed. By this criterion, the first five eigenvalues and EOF's are considered to be significant, and the eigenvalues and EOF's from rank six and beyond cannot be

distinguished unambiguously. One notes that the eigenvalues for EOF's 2 and 3 do not have the required separation. However, examination of their maps, coefficient time histories, and spectra will indicate that they are physically meaningful.

Maps of the first five EOF's, their coefficient histories (the $\underline{u}_k$ and the α_{ik}, respectively) and the resulting temporal spectra are shown in Figs. 1 through 5. Each coefficient history begins in July 1975. The four missing months during the gap between Nimbus-6 and Nimbus-7 ERB are marked by asterisks in the time histories; when determining the spectra, these values were replaced by the long-term means for their respective months. To facilitate intercomparisons, the maps are normalized such that the maximum absolute value which occurs is 1. The true value of the EOF can be recovered by multiplying the map value by the normalization factor listed in Table 2.

The first EOF accounts for 65.7% of the variance and is seen in Fig. 1 to be mainly an annual cycle, although there is a small non-annual part present. It follows the solar heating with a small phase lag, and is basically a summer winter cycle. The temperate latitudes of the hemispheres differ in sign. The largest variation in EOF 1 is over Central Asia; the strongest centers in both the Tropics and midlatitudes are on or at the borders of continents. The OLR over Central Asia, as at other points in the middle and high latitudes, responds to changes in surface temperature and boundary layer emission, which track solar heating. Over the Tropics and subtropics, the seasonal temperature changes are much smaller than at the higher latitudes. The low latitude OLR responds to the movements of large cloud patterns which are in turn

forced by seasonal changes in air flow and moisture. An increase in surface temperature produces an increase in OLR, but an increase in cloudiness decreases OLR; this accounts for the difference in sign within a hemisphere between the low and high latitudes in EOF 1. The large difference between the emitting temperatures of the high clouds found in the Tropics and tropical surfaces explains the low latitude dominance in these maps.

The first EOF is in good agreement with Heddinghaus and Krueger (1981), who found a variance of 66.2% associated with it. A curious feature of the first EOF coeffi- cient vector is the modulation of the amplitude envelope with an apparent period of 11 to 12 years. The coefficient vector of the 6th EOF varies with the same apparent period and phase.

The second EOF accounts for variance of 4.6%, which is less than the first by an order of magnitude. Fig. 2 shows it is also largely an annual cycle, but with a significant semiannual part and an interannual part present. It is to be expected that two EOF's would be associated with the annual cycle in order to represent regions with differing phases. The second EOF accounts for most of the annual cycle which is out of phase with EOF 1 and is a cycle which peaks in spring and fall, i.e., April and November. These results are very similar to those found by G. L. Smith and Bess (1983) for the cosine and sine parts of the annual cycle. Following the peak in November, the coefficient rapidly falls to the April minimum, producing the semiannual component with non-sinusoidal behavior.

EOF 2 appears as a seesaw between the central-eastern Pacific Ocean and the Indian Ocean-Indonesia regions, which are at opposite ends of the Walker circulation. The extreme negative component of the seesaw maps the fall position of the Intertropical Convergence Zone (ITCZ) near Southeast Asia and the Phillipine Sea; the fall ITCZ stretches across the Pacific Ocean to the Atlantic Ocean where it is weaker. The negative lobe also matches the position of the southeast Asia 200-mb anticyclone which substantially weakens after November. The positive lobe is over the central equatorial Pacific Ocean. It corresponds to a spring maximum in cloudiness which is related to seasonal variations in sea surface temperature and low level convergence (Horel, 1982). Meehl (1987, 1988) points out that the monsoon is stronger in the southerly transit during July to January than in the northerly transit; the Asian lobe of EOF 2 is consistent with increased cloudiness associated with the monsoon by indicating an OLR minimum during Northern Hemisphere fall. The midlatitude positive maxima over the north Atlantic and north Pacific Oceans coincide with the annual cycle of sea-surface temperature; these maxima are present, but much weaker in the Southern Hemisphere. The Antarctic has a fairly strong signal, indicating a significant spring-fall mode. Hsu and Wallace (1976) found a spring-fall trend in Antarctic sea level pressure, but it does not appear in surface temperature (White and Wallace, 1978), so the OLR effect likely results from cloudiness. The annual cycle of Antarctic sea level pressure has a maximum in Northern Hemisphere spring; this maximum may produce a cloud signal that accounts for the corresponding maximum in OLR which is found here.

The relatively weak maximum in the equatorial Atlantic near the Amazon was the predominant feature of the EOF 2 of Heddinghaus and Krueger (1981). In the present data set, EOF 2 has a strong center of action over the equatorial Pacific Ocean; this center was only weakly indicated in Heddinghaus and Krueger (1981). Thus, while the SR conversion algorithm (used by Heddinghaus and Krueger, 1981) apparently captures the summer-winter variations (EOF 1), it misses the full strength of an important spring-fall mode in the tropical Pacific (EOF 2). This problem is apparently due to the lack of correlation of water vapor in the Tropics with atmospheric temperature which is required for the SR conversion algorithm to work well. In the present record, EOF 2 has a noteworthy anomaly in months 93 and 94 of the record (March and April, 1983), where its peak signal changes by over 40 $W\text{-}m^{-2}$ (multiply the peak -1.0 in Fig. 2a by -10 in Fig. 2b, and then by the normalization factor 4.11 in Table 2), rather than approximately 28 $W\text{-}m^{-2}$ as for most Februarys. The anomaly was produced by the 1982-83 El Niño-southern oscillation (ENSO) event. The anomaly in EOF 2 did not appear in the 1976-77 ENSO because that ENSO occurred at a different time of the year.

Examination of the time history of cofficient 3 in Fig. 3 shows it to be heavily dominated by a semiannual cycle. EOF 3 has strong centers of monsoonal action located over India and the Timor Sea. There are several areas of moderate strength but out of phase with the monsoonal activity. Much of the Earth is relatively unaffected. The Antarctic is seen to have a significant variation, which is consistent with semiannual cycles in surface temperature (White and Wallace, 1978) and

in sea level pressure (Hsu and Wallace, 1976) over the Antarctic. EOF 3 of the present study is very similar to EOF 3 of Heddinghaus and Krueger (1981). In the present data set, EOF 3 accounts for 3.8% of the variance, whereas Heddinghaus and Krueger (1981) found 4.1%. The difference is attributed here to the difference of spatial domains used for the analyses.

Fig. 4 shows that EOF 4 has strong interannual and semiannual parts. It has strong centers of action over the central equatorial Pacific Ocean and New Guinea, which are out of phase. Other areas along the Equator also show significant signals, as does Antarctica. The peaks of its time history correspond to ENSO episodes, so it seems reasonable to identify this EOF as the dominant EOF mode for describing an ENSO. The 1982-83 ENSO episode was so strong that it stands out in Fig. 4b as a unique feature. This feature is roughly a triangle in appearance, which would be described by a spectrum which is flat out to the frequency corresponding to the width of the feature, beyond which it is red except for a semiannual spike at 0.167 $year^{-1}$, as seen in Fig. 4c. Both Heddinghaus and Krueger (1981) and the present work place 2.9% of the variance in EOF 4. This agreement is fortuitous. Heddinghaus and Krueger (1981) used 45 months of data that contained one ENSO event (1976-77). Here, we use a record with 120 months, about three times that of Heddinghaus and Krueger (1981), which contains two ENSO events (1976-77 and 1982-83). The second ENSO was about twice as strong as the first, so that we obtain the same variance in ENSO events per unit time.

The dominant feature of EOF 5 is a strong center near Java and a region of opposite sign which extends across the Pacific Ocean from New

Guinea to North America. Another feature extends from the Himalayas across Africa to the south Atlantic Ocean. Also, there are centers over the Caribbean Sea and the Antarctic. The power spectrum of EOF 5 is nearly flat except for a weak semiannual peak. As a consequence, this EOF is a mixture of semiannual responses and patterns corresponding to month-to-month variations. The shape of EOF 5 indicates an effect of the seasonal passage of the monsoon from Asia to Australia and back. The coefficent is positive for each August of the record, which indicates a high OLR to the west of the monsoon track (and low to the east) as it first moves southward. The same pattern is produced in early Northern Hemisphere spring when the monsoon begins to move northward, though not with the same consistency. The "dipole straddling" of the monsoon track is more consistent when the Sun is in the Northern Hemisphere. The greater consistency is in agreement with the stronger Northern Hemisphere monsoon which is indicated by EOF 1.

Some interesting relationships exist between EOF maps 4 and 5. The extrema of EOF 4 near Indonesia and the central Pacific Ocean, which form a dipole, are shifted in EOF 5 to the west by 90°. A dipole which appears shifted between two EOF's suggests a moving wave. Lau and Chan (1985) noted the pronounced OLR signal of 40-50 day oscillations in this area. The time-lagged cross correlation of the coefficients of EOF's 4 and 5 is shown in fig. 6, which shows that EOF 4 leads EOF 5 by 4 to 6 months with a correlation coefficient of 0.4. For zero time lag, the correlation vanishes because the cofficients of EOFs are required to be uncorrelated. For EOF 4 lagging EOF 5, the sign changes, and the correlation peaks at 4 months with a value of -0.4.

The time history of EOF 6 suggests a cycle of approximately a 1-decade period. Its time spectrum also shows a strong peak at the 1-decade period and another strong peak at the semiannual cycle. Time histories and spectra for EOF 7 through 10 are not discernible from white noise. The maps, however, show major features in the Indian Ocean and Indonesia-New Guinea regions, indicating that the EOF's themselves are real patterns rather than spatial white noise, and that a large part of the variation in monthly averaged OLR maps is in the Tropics. The variance associated with EOF 6 is 1.9%, so the present authors are reluctant to attribute much significance to details of this EOF.

In examining the maps of the first 10 EOF's, the major impression is that most of the EOF's of rank 3 and greater are describing variations primarily in the region near the Equator from India to the Pacific Ocean just east of New Guinea, and to a lesser extent their statistical relations to smaller changes elsewhere over the globe. The mid- and high-latitude variations are primarily summer-winter variations described by EOF 1. The response of the middle and high latitudes becomes progressively smaller as one goes from the first EOF to EOF's of increasing order; however, significant signals over Antarctica are found out to EOF 6.

An EOF analysis was also done on the OLR data with a "canonical" seasonal cycle. The canonical cycle was formed of average January, average February, etc., and consisted of 12 time steps. The variances contained in the canonical EOF's are found in Table 3. Maps of the first four canonical EOF's (not displayed) show very close correspondence to the regular EOF's 1, 2, 3, and 5, respectively.

In order to enhance the visibility of any interseasonal and interannual variations, the annual cycle was removed from the data sets in order to prewhiten the data so that the annual and semiannual cycles would not dominate the spectra. The resulting eigenvalues are listed in Table 1. It is found that the first three eigenvalues are significant, and rank 4 and beyond cannot be meaningfully distinguished.

The first three EOF's for the season removed are shown in Figs. 7 through 9, along with their time histories and spectra. The spectra of EOF's 1 and 2 with seasonal cycle removed have strong interannual components over a wide range. It is seen that the maps for EOF's 1 and 2 with the seasonal cycle removed resemble very closely EOF's 4 and 6 with the seasonal cycle left in. Heddinghaus and Krueger (1981) found that their first non-seasonal EOF corresponded to their EOF 4 with the season left in. Also, the histories of the coefficients of EOF's 4 and 6 with season resemble those of EOF's 1 and 2 without seasonal cycle quite much. (Note that the sign of an EOF or its coefficent vector is arbitrary; however, they must be consistent so that their product is uniquely defined.)

Deseasonalized EOF 1 (Fig. 7) has the classical ENSO pattern over the equatorial Pacific Ocean with secondary lobes in the subtropical central Pacific Ocean and over the equatorial Atlantic Ocean. This EOF and EOF 4 (Fig. 4) without season removed are seen to differ over the region of India and the Arabian Sea and over Antarctica. This difference probably results from the annual and semiannual components in the coefficient vector of EOF 4.

Deseasonalized EOF 2 has a center of action on the Equator at 160E, where a persistent increase of OLR following the 1982-83 ENSO event is

noted. A comparison of the most extreme months (October 1975 and 1977) of the Nimbus 6 WFOV record with SR data (Winston et al., 1979) shows that both records have anomalously high OLR in October 1975 and low values in October 1977.

The deseasonalized EOF 3 shows a change in level coinciding with the change from Nimbus 6 to Nimbus 7 data in 1978, which causes the peak in the spectrum at a decade. The center of action of EOF 3 is over the equatorial Indian Ocean. No significant asymmetry between continents and oceans or between hemispheres is seen.

The autocorrelations of these deseasonalized EOF's are shown in Fig. 10. EOF's 1 and 2 appear to be nearly exponential, so that they could perhaps be modeled as Markovian. At 6 months they still have autocorrelations of 0.2. The autocorrelation of EOF 3 shows two effects. The first effect approximates an exponential decrease with characteristic time of about 3 months, and the second is a long-term effect, which is the change in level in late 1978.

Fig. 11 shows the time-lagged correlation coefficient between pairs of deseasonalized EOF's. Deseasonalized EOF's 1 and 2 show the same correlation behavior at lead and lag as do EOF's 4 and 5 without removal of season. EOF's 2 and 3 have correlations of -0.2 to -0.3 for lag-lead times of 1 to 5 months.

4. Conclusions

The method of empirical orthogonal functions has been demonstrated by application to a 10-year data set of outgoing longwave radiation. It is seen that the EOF's provide a method for analyzing a time series of maps. Also, spherical harmonic functions are a suitable basis set for producing equal area map results. The following findings are noted:

1. The first EOF accounts for 66% of the variance. After that, the EOF's each account for only a small variance, forming a slowly converging series.

2. The first two EOF's describe mainly the annual cycle.

3. The third EOF is primarily the semiannual cycle although many other EOF's also contain significant semiannual parts.

These three results reaffirm those of Heddinghaus and Krueger (1981). In addition, the following items were found:

4. A much stronger spring/fall mode (EOF 2) was found in the central equatorial Pacific Ocean. The earlier narrowband measurements did not capture the strength of this feature.

5. The third through sixth EOF each capture some of the significant semiannual variations in OLR found over Anarctica.

6. The fourth EOF describes much of the 1982-83 ENSO phenomenon.

7. The fifth EOF has interannual and semiannual contributions. We have found an OLR dipole that apparently straddles the southeast Asia-Australia monsoon track; this effect is semiannual with variations in intensity from year to year.

8. There is typically a gap in the spectrum between a semiannual peak and the annual cycle for all but the first EOF.

9. The first EOF with annual cycle removed describes the ENSO events of 1976-77 and 1982-83.

10. The second EOF with annual cycle removed describes a post ENSO feature, primarily an anomalously high OLR at 160^{o}E on the Equator, following the ENSO's of 1976-77 and 1982-83.

5. Appendix: EOF Relations between Spherical Harmonic and Grid Point Bases

In this appendix, we demonstrate relations between EOF's in the spherical harmonic and grid point systems which permit their computation in the spherical harmonic system and subsequent mapping to the grid system. This approach is more economical and preserves accuracy as compared to mapping first to the grid system and then computing the EOF's.

The spherical harmonic coefficients for a given month i form a vector $\underline{h}_i$, and the deviation

$$\underline{z}_i = \underline{h}_i - \langle \underline{h} \rangle \tag{A1}$$

is computed. The OLR fields in the grid and spherical harmonic systems are related by

$$x_{ip} = \sum_q Y_q(p)\, z_{iq} \tag{A2}$$

where $Y_q(p)$ is the spherical harmonic function of order and degree denoted by the single index q, evaluated at point p, and z_{iq} is the q-th coefficient for the i-th month. This relation may be written in matrix form as

$$\underline{x}_i = A\, \underline{z}_i \tag{A3}$$

By the orthogonality of the spherical harmonic functions, the z_{iq} may be be written in terms of the x_{ip} as

$$z_{iq} = \int_0^{2\pi} d\phi \int_0^{\pi} d\theta \, \sin\theta \, Y_q^*(p)\, x_{ip} \tag{A4}$$

In this equation only, the p is used to denote points which are continuously distributed over the sphere; elsewhere p denotes grid

points. In practice, a finite grid size will be used to evaluate this integral, so that it is approximated by the finite sum

$$z_{iq} = \sum_{p} \Delta S \; Y_q^*(p) \; x_{ip} \qquad \text{(A5)}$$

It is seen that if and only if the ΔS are constant for all grid elements, then eq. (9) may be written in matrix form as

$$\underline{z} = \Delta S \; A^* \; \underline{x} \qquad \text{(A6)}$$

In order to avoid A being singular, we will assume that the number of grid elements equals the number of spherical harmonic coefficients. This assumption is not a necessity, but a convenience. It is seen that the orthogonality of the spherical harmonics results in the relation

$$\Delta S \; A^* \; A = I \qquad \text{(A7)}$$

where I is the identity matrix. A rotation matrix is characterized by the property that its inverse is its adjoint; thus the transformation A may be regarded as a rotation in function space from the grid system to the spherical harmonic system, provided that the grid elements are of equal area.

In order to compute the EOF's in the spherical harmonic system, the covariance V of the $\underline{z}$ is computed:

$$V = \frac{1}{I} \sum_{i=1}^{I} \underline{z}_i \underline{z}_i^t \qquad \text{(A8)}$$

and the EOF's and their associated variances using the spherical harmonic coefficients as a basis set can be computed:

$$V \; \underline{w}_k = \mu_k \underline{w}_k \qquad \text{(A9)}$$

It is noted that this procedure is equivalent to solving the Karhunen-Loève equation (Papoulis, 1965) on a sphere:

$$\int_{4\pi} dS\ \Gamma(p,p')\ \psi(p') = \lambda\ \psi(p)$$

in which $\Gamma(p,p')$ is the covariance function for the x field:

$$\Gamma(p,p') = \langle x(p)\ x(p') \rangle$$

where $< >$ denotes the expected value. The sample covariance function may be expressed in terms of the covariance matrix V as

$$\Gamma(p,p') = \sum_m \sum_n Y_m(p)\ V_{mn}\ Y_n^*(p')$$

Thus, eq. (A9) is simply the Karhunen-Loève equation expressed on a spherical harmonic basis.

It is now demonstrated that the EOF's $\underline{w}_k$ in the spherical harmonic system are related to the EOF's $\underline{u}_k$ in the grid system by the transformation A, i.e.,

$$\underline{u}_k = A\ \underline{w}_k \qquad \text{(A10)}$$

Eqs. (A3) and (A8) are used in eq. (1) to relate the covariance matrix C in the grid system to V by the similarity transformation

$$C = A\ V\ A^* \qquad \text{(A11)}$$

Eqs. (A10) and (A11) are now substituted into eq. (A9) to give

$$A\ V\ A^* A\ \underline{w}_k = \lambda_k\ A\ \underline{w}_k \qquad \text{(A12)}$$

This eq. is true if and only if A^*A is the identity matrix times a scalar. This relation is given by eq. (A7) for the case of equal area grid elements only, in which case the scalar is $(\Delta S)^{-1}$. Furthermore, the eigenvalues in the two systems are related by

$$\lambda_k = \Delta S\ \mu_k \qquad \text{(A13)}$$

If equal area grid elements are not used, the relationship does not hold.

In this paper, the EOF's are computed by use of eq. (A9), so that they are on the equal area basis. These EOF's are then mapped into a latitude-longitude map.

6. References

Bess, T. D. and Smith, G. L., 1987a: Atlas of wide-field-of-view outgoing longwave radiation derived from Nimbus 6 Earth radiation budget data set - July 1975 to June 1978, NASA Reference Publication 1185.

Bess, T. D. and Smith, G. L., 1987b: Atlas of wide-field-of-view outgoing longwave radiation derived from Nimbus 7 Earth radiation budget data set - November 1978 to October 1985, NASA Reference Publication 1185.

Heddinghaus, T. R. and Krueger, A. F., 1981: Annual and interannual variations in outgoing longwave radiation over the tropics. Mon. Wea. Rev., 109, 1208-1218.

Horel, J. D., 1982: On the annual cycle of the tropical Pacific atmosphere and Ocean. Mon. Wea. Rev., 110, 1863-1878.

Horel, J. D. and J. M. Wallace, 1981: Planetary scale atmospheric phenomona associated with the southern oscillation. Mon. Wea. Rev., 109, 800-807.

Holmstrom, I., 1970: Analysis of time series by means of empirical orthogonal functions. Tellus, 27, 638-647.

House, F. B., A. Gruber, G. E. Hunt and A. T. Mecherikunnel, 1986: History of satellite missions and measurements of the Earth's radiation budget (1957-1984), Rev. Geophys., 24, 357-377.

Hunt, G. E., R. Kandel and A. T. Mecherikunnel, 1986: A history of presatellite investigations of the Earth's radiation budget, Rev. Geophys., 24, 351-356.

Hsu, C.-P. F. and J. M. Wallace, 1976: The global distibution of the annual and semiannual cycles in sea level pressure, Mon. Wea. Rev., 104, 1597-1601.

Jacobowitz, H., H. V. Soule, H. L. Kyle, F. B. House and the NIMBUS 7 ERB Experiment Team, 1984: The Earth radiation budget (ERB) experiment: An overview. J. Geophys. Res., 89, No. D4, 5021-5038.

Kutzbach, J., 1967: Empirical eigenvectors of sea level pressure, surface temperature, and precipitation complexes over North America. J. Appl. Meteor., 6, 791-802.

Lau, K. M. and P. H. Chan, 1985: Aspects of the 40-50 day oscillation during northern winter as inferred from outgoing longwave radiation. Mon. Weather Rev., 113, 1889-1909.

Lau, K. M. and P. H. Chan, 1986: The 40-50 day oscillation and the El Nino/southern oscillation: a new perspective. Bull. Amer. Met. Soc., 67, 533-534.

Meehl, G. A., 1987: The annual cycle and interannual variability in the tropical Pacific and Indian Ocean regions, Mon. Wea. Rev., 115, 27-50.

Meehl, G. A., 1988: Tropical mid-latitude interactions in the Indian and Pacific sectors of the Southern Hemisphere, Mon. Wea. Rev., 116, 472-484.

North, G. R., T. L. Bell, R. F. Cahalan and F. J. Moeng, 1982: Sampling errors in the estimation of empirical orthogonal functions, Mon. Weath. Rev., 110, 699-706.

Papoulis, A., 1965: Probability, Random Variables and Stochastic Processes, McGraw-Hill, New York.

Smith, G. L. and Bess, T. D., 1983: Annual cycle and spatial spectra of Earth-emitted radiation at large scales, J. Atmos. Sci., 40, 998-1015.

Smith, G. L. and R. N. Green, 1981: Deconvolution of wide-field-of-view radiometer measurements of Earth-emitted radiation. Part I. Theory. J. Atmos. Sci., 38, 461-473.

Smith, W. L., J. Hickey, H. B. Howell, H. Jacobowitz, D. T. Hilleary and A. J. Drummond, 1977: Nimbus 6 Earth radiation budget experiment. Appl. Opt., 16, 306-318.

Wallace, J. M. and D. S. Gutzler, 1981: Teleconnections in the geopotential height field during the Northern Hemisphere winter. Mon. Wea. Rev., 109, 785-812.

White, G. H. and J. M. Wallace, 1978: The global distribution of the annual and semiannual cycles in surface temperature, Mon. Weath. Rev., 106

Winston, J. S., A. Gruber, T. I. Gray, Jr., M. S. Varnadore, C. L. Earnest and L. P. Manello, 1979: Earth-atmosphere radiation budget analysis derived from NOAA satellite data, June 1974-February 1978, vols. 1 and 2. NOAA, 34pp.

Table 1. - Percentages of variance explained by each empirical orthogonal function.

	annual cycle present		noise	annual cycle removed		noise
rank	%variance	cumulative	est.	%variance	cumulative	est.
1	65.7	65.7	12.0	12.8	12.8	2.3
2	4.6	70.2	.8	8.4	21.2	1.5
3	3.8	74.0	.7	6.2	27.4	1.1
4	3.0	77.0	.5	4.6	31.9	.8
5	2.3	79.2	.4	4.4	36.3	.8
6	1.9	81.1	.3	4.3	40.6	.8
7	1.2	82.4	.2	3.3	43.9	.6
8	1.1	83.4	.2	3.1	47.0	.6
9	1.0	84.4	.2	2.6	49.6	.5
10	.9	85.3	.2	2.4	52.1	.5

Table 2. - Normalization factors for mapped EOFs

rank	annual cycle present	annual cycle removed
1	2.85	5.27
2	4.11	5.06
3	4.46	3.26
4	4.59	3.94
5	3.49	4.84
6	4.42	3.55

Table 3. - Percentages of variance explained by each empirical orthogonal function for "canonical" seasonal cycle

	annual cycle present		type
rank	%variance	cumulative	
1	86.0	86.0	summer-winter
2	5.3	91.3	spring-fall
3	4.4	95.7	semiannual
4	2.0	97.7	semiannual
5	.7	98.4	
6	.6	99.0	
7	.3	99.3	
8	.2	99.5	
9	.2	99.7	
10	.2	99.9	

LIST OF FIGURES

Figure 7. Empirical orthogonal function 1 of OLR fields with seasonality removed: Map, time history and temporal spectrum.

a. Map of empirical orthogonal function 1 for seasonality removed

b. Time history of empirical orthogonal function 1 for seasonality removed.

c. Spectrum of empirical orthogonal function 1 for seasonailty removed.

Figure 8. Empirical orthogonal function 2 of OLR fields with seasonality removed: Map, time history and temporal spectrum.

a. Map of empirical orthogonal function 2 for seasonality removed

b. Time history of empirical orthogonal function 2 for seasonality removed.

c. Spectrum of empirical orthogonal function 2 for seasonality removed.

Figure 9. Empirical orthogonal function 3 of OLR fields with seasonality removed: Map, time history and temporal spectrum.

a. Map of empirical orthogonal function 3 for seasonality removed

b. Time history of empirical orthogonal function 3 for seasonality removed.

c. Spectrum of empirical orthogonal function 3 for seasonality removed.

Figure 10. Autocorrelation for EOF's computed with seasonal cycle removed.

Figure 11. Time-lagged cross correlation coefficents for EOF's computed with seasonal cycle removed.

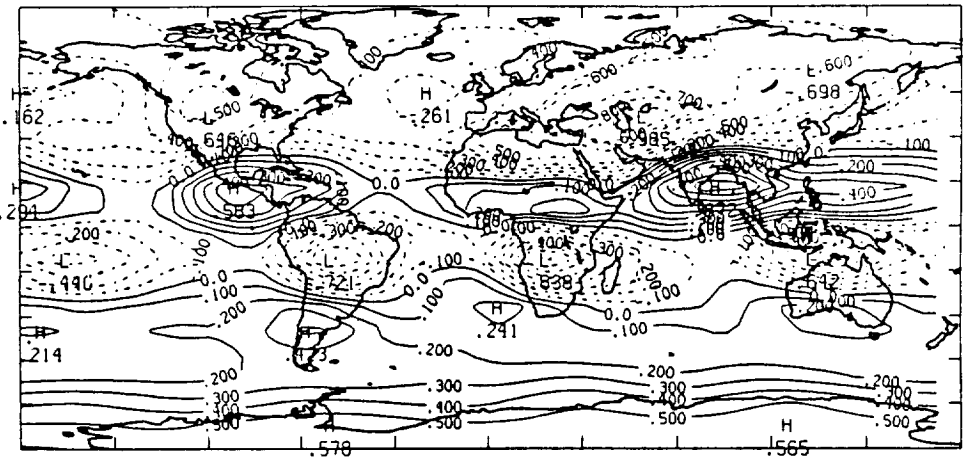

a. Map of empirical orthogonal function 1.

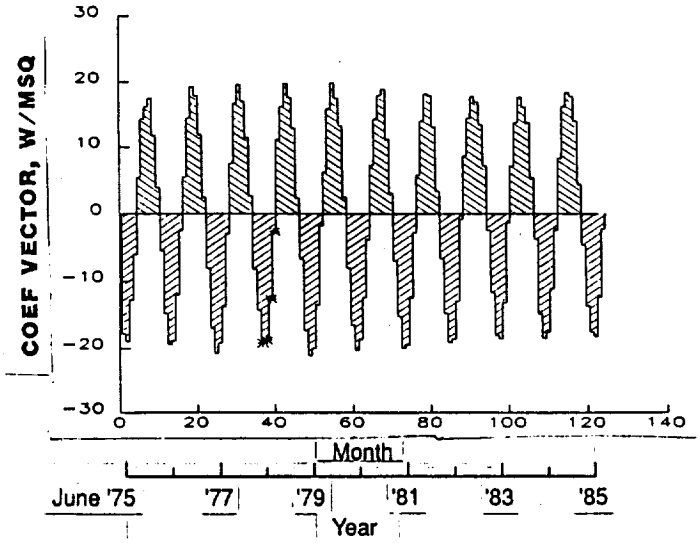

b. Time history of empirical orthogonal function 1.

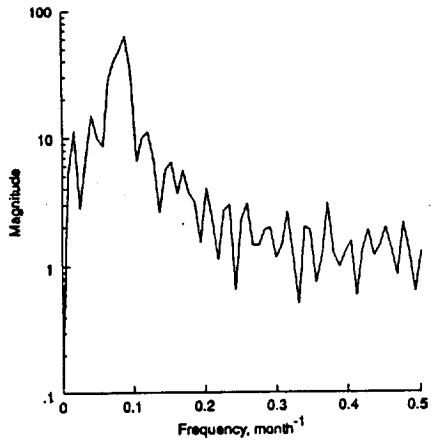

c. Spectrum of empirical orthogonal function 1.

Figure 1. Empirical orthogonal function 1: Map, time history and temporal spectrum.

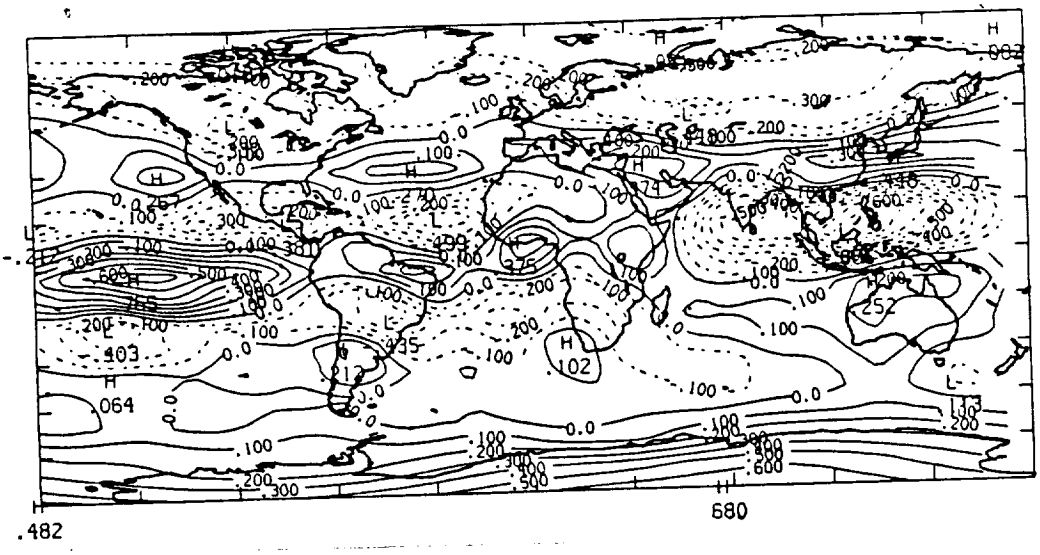

a. Map of empirical orthogonal function 2.

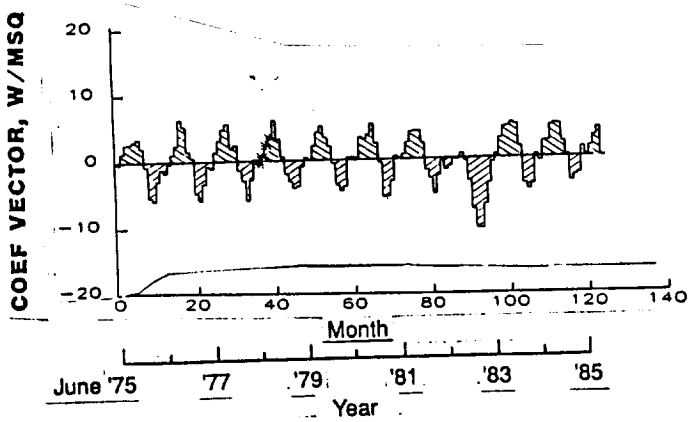

b. Time history of empirical orthogonal function 2.

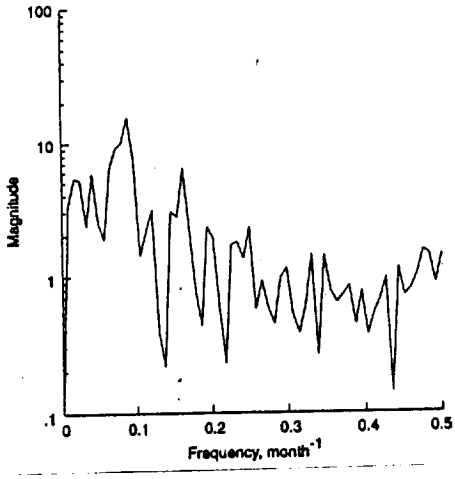

c. Spectrum of empirical orthogonal function 2.

Figure 2. Empirical orthogonal function 2: Map, time history and temporal spectrum.

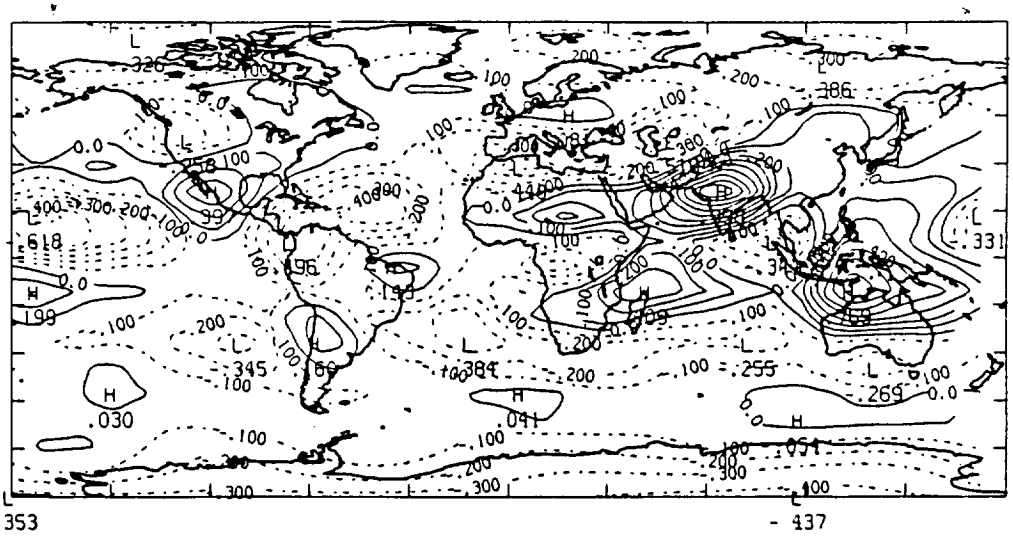

a. Map of empirical orthogonal function 3.

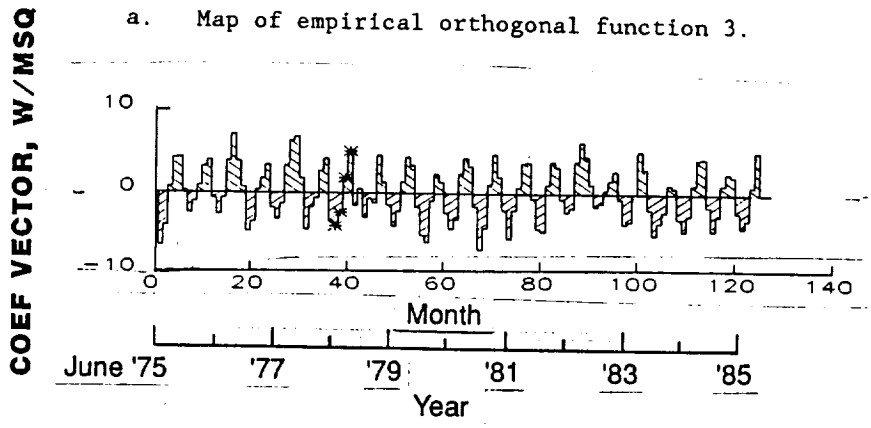

b. Time history of empirical orthogonal function 3.

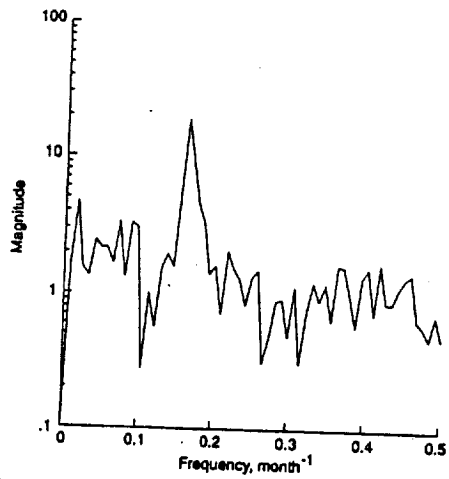

c. Spectrum of empirical orthogonal function 3.

Figure 3. Empirical orthogonal function 3: Map, time history and temporal spectrum.

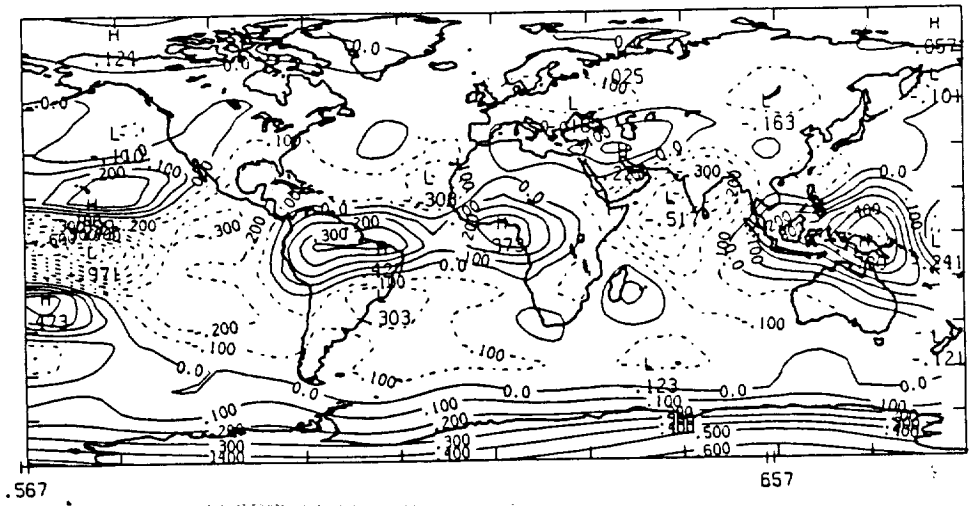

a. Map of empirical orthogonal function 4.

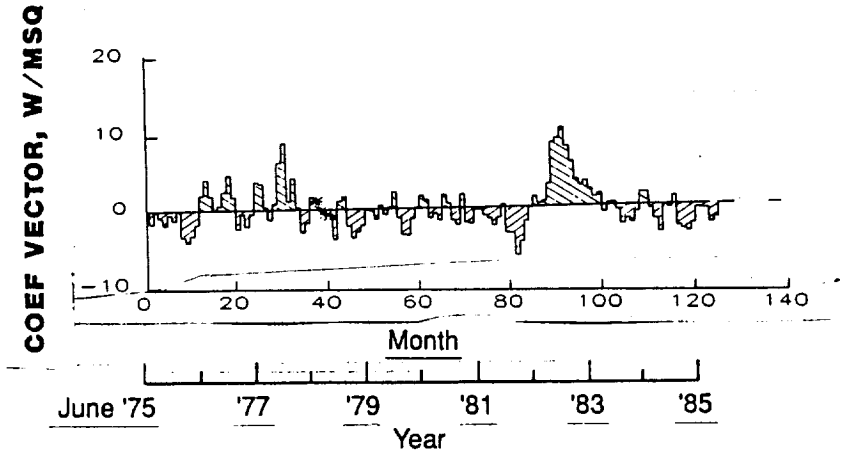

b. Time history of empirical orthogonal function 4.

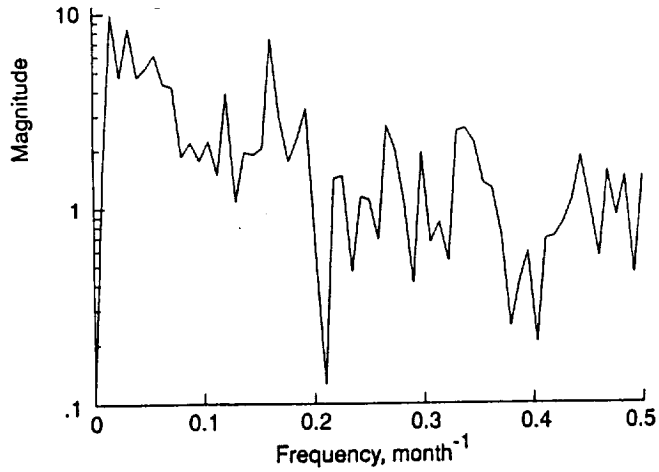

c. Spectrum of empirical orthogonal function 4.

Figure 4. Empirical orthogonal function 4: Map, time history and temporal spectrum.

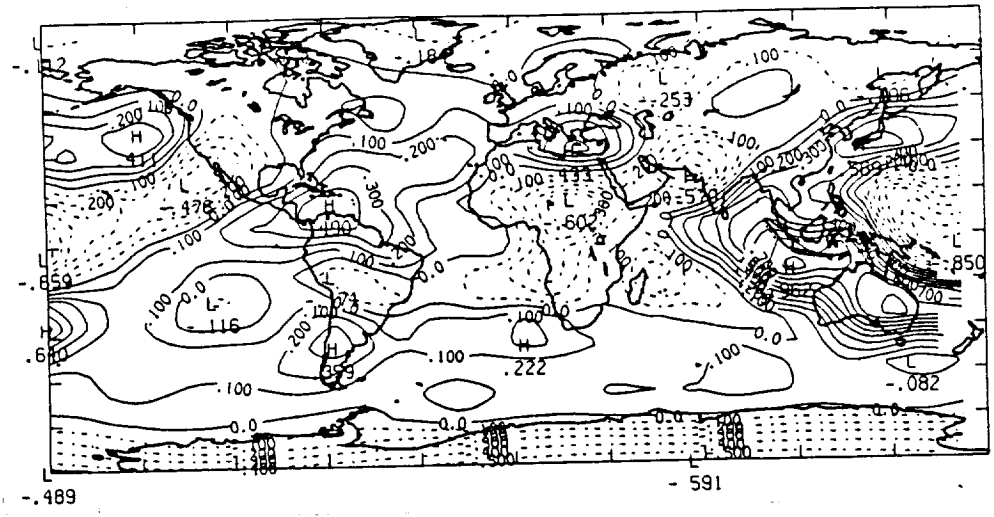

a. Map of empirical orthogonal function 5.

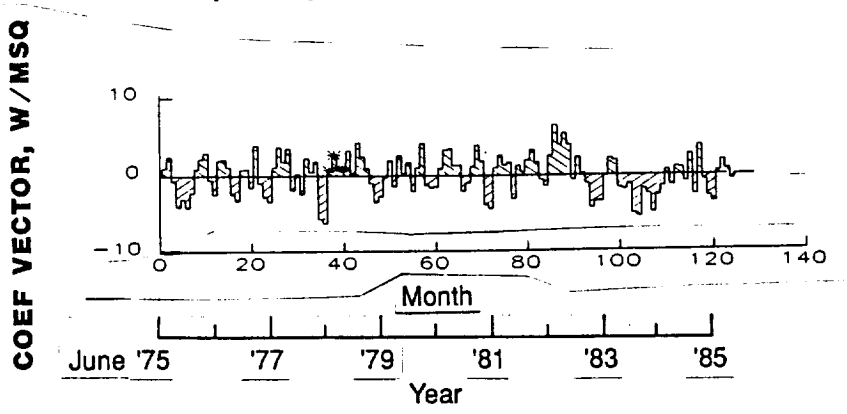

b. Time history of empirical orthogonal function 5.

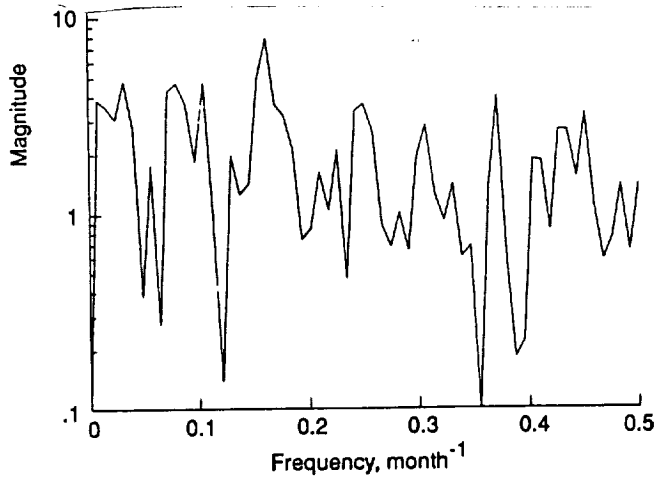

c. Spectrum of empirical orthogonal function 5.

Figure 5. Empirical orthogonal function 5: Map, time history and temporal spectrum.

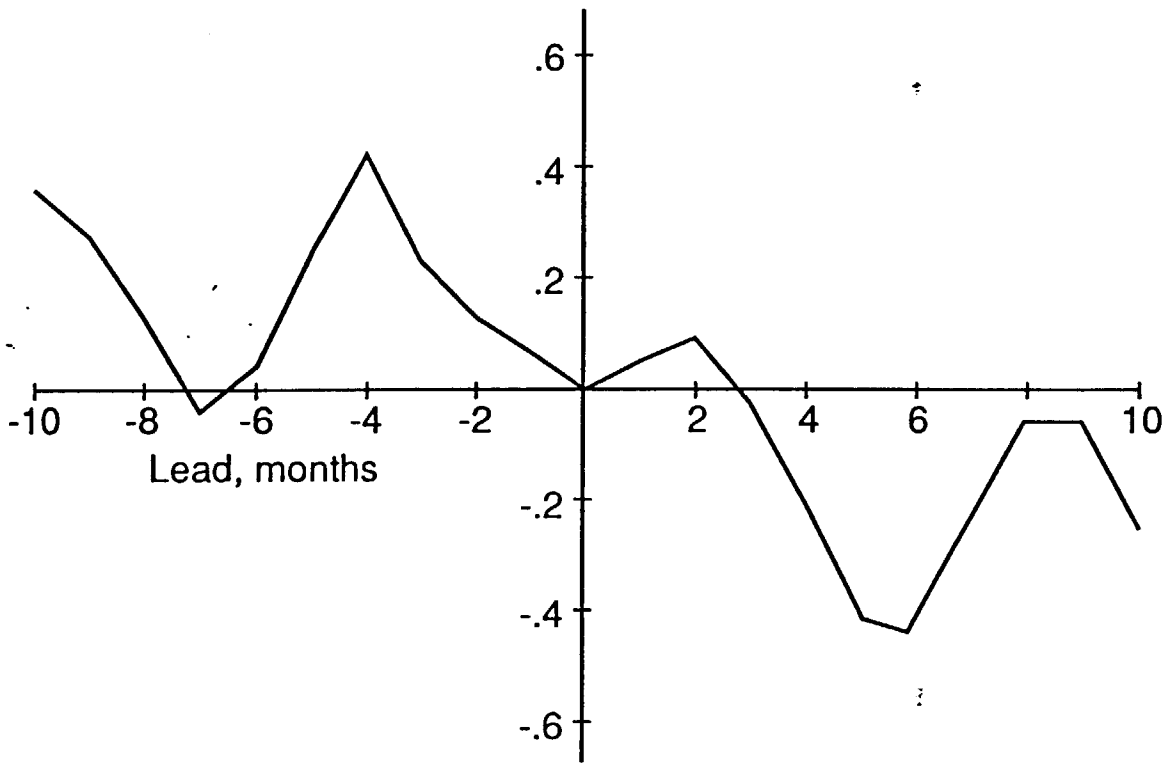

Figure 6. Time-lagged correlation for EOF's 4 and 5.

Fig 6

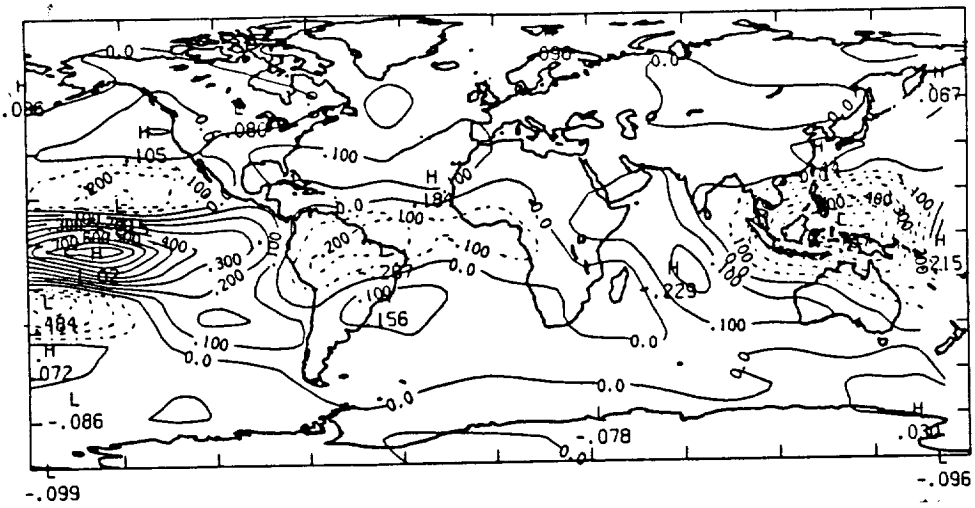

a. Map of empirical orthogonal function 1 for seasonality removed

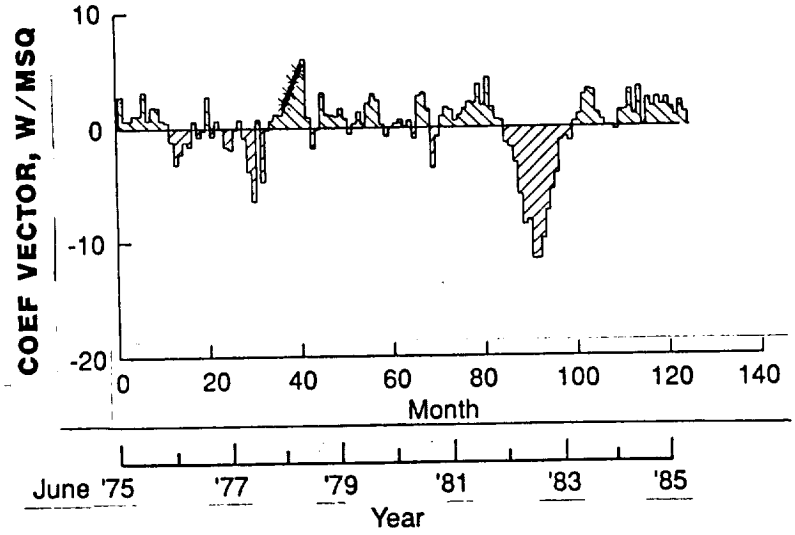

b. Time history of empirical orthogonal function 1 for seasonality removed.

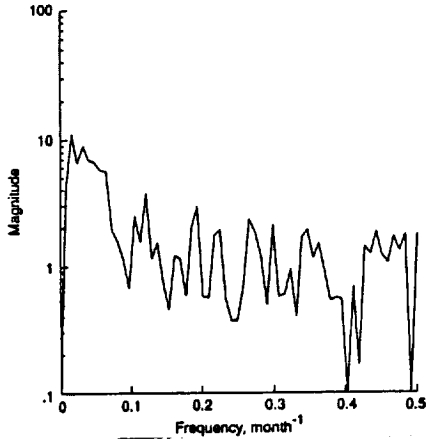

c. Spectrum of empirical orthogonal function 1 for seasonailty removed.

Figure 7. Empirical orthogonal function 1 of OLR fields with seasonality removed: Map, time history and temporal spectrum.

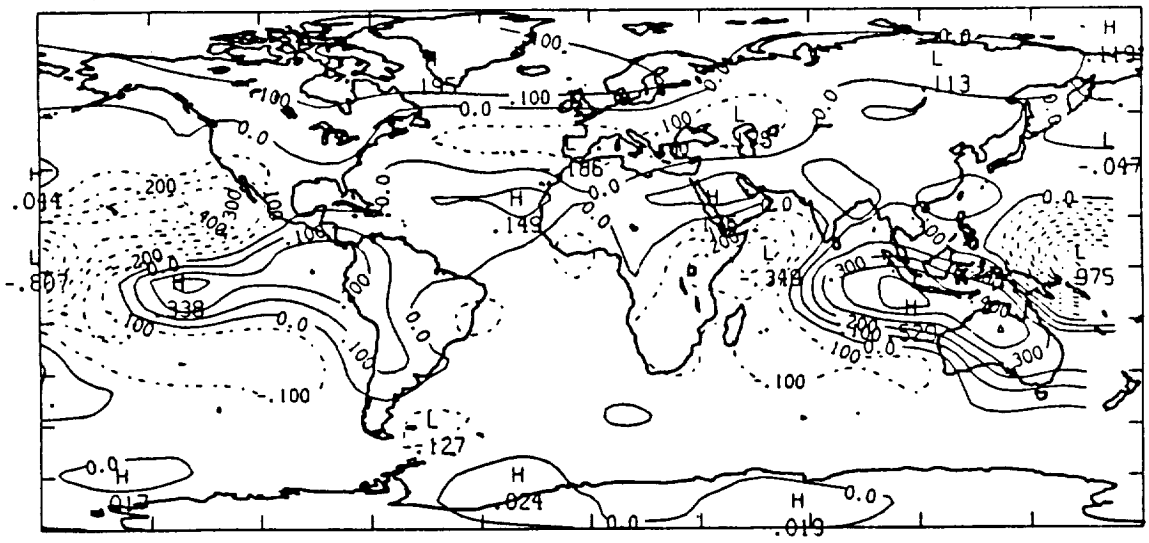

a. Map of empirical orthogonal function 2 for seasonality removed

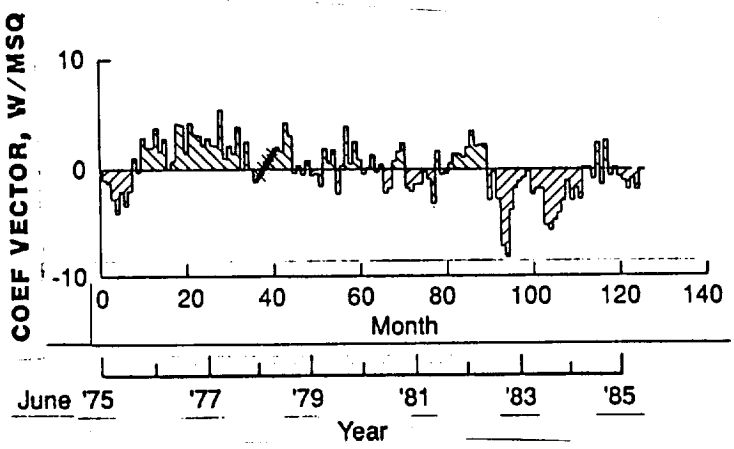

b. Time history of empirical orthogonal function 2 for seasonality removed.

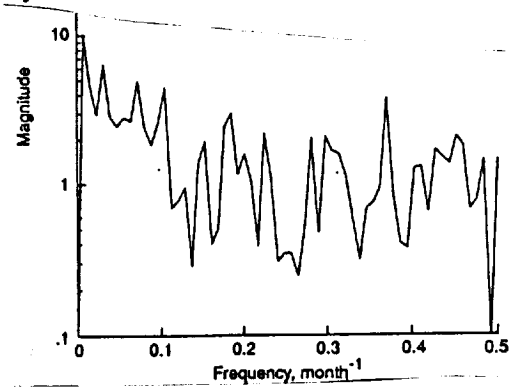

c. Spectrum of empirical orthogonal function 2 for seasonality removed.

Figure 8. Empirical orthogonal function 2 of OLR fields with seasonality removed: Map, time history and temporal spectrum.

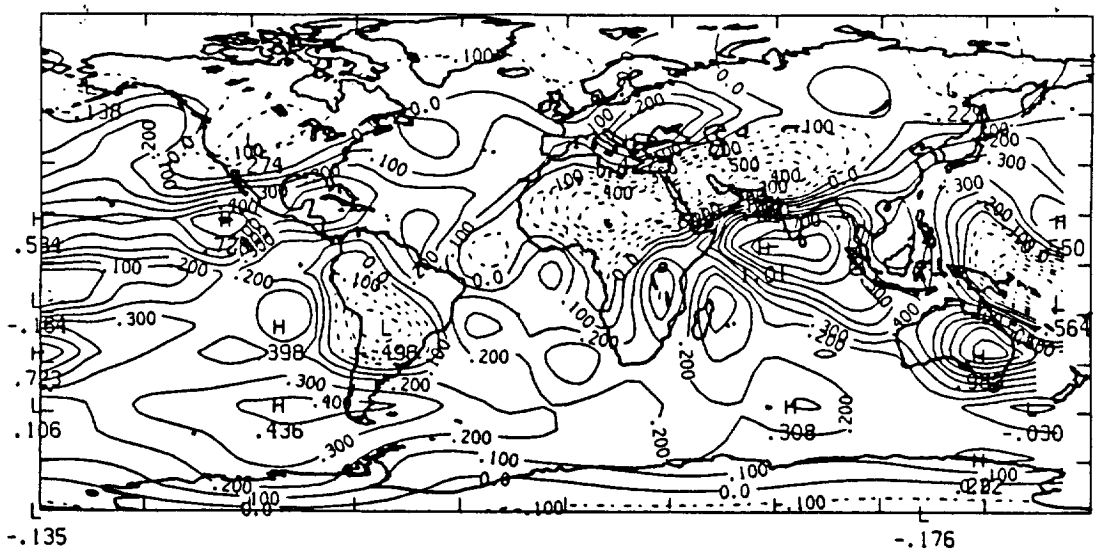

a. Map of empirical orthogonal function 3 for seasonality removed

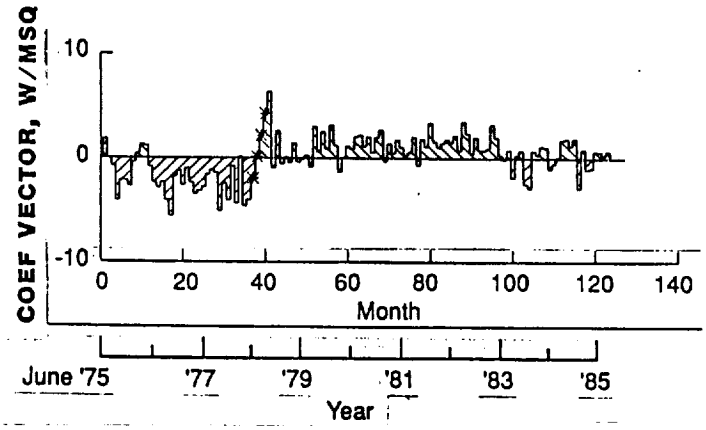

b. Time history of empirical orthogonal function 3 for seasonality removed.

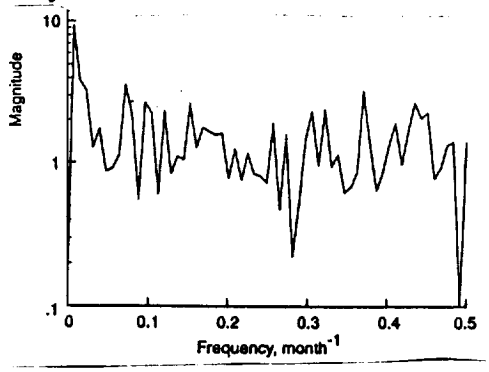

c. Spectrum of empirical orthogonal function 3 for seasonality removed.

Figure 9. Empirical orthogonal function 3 of OLR fields with seasonality removed: Map, time history and temporal spectrum.

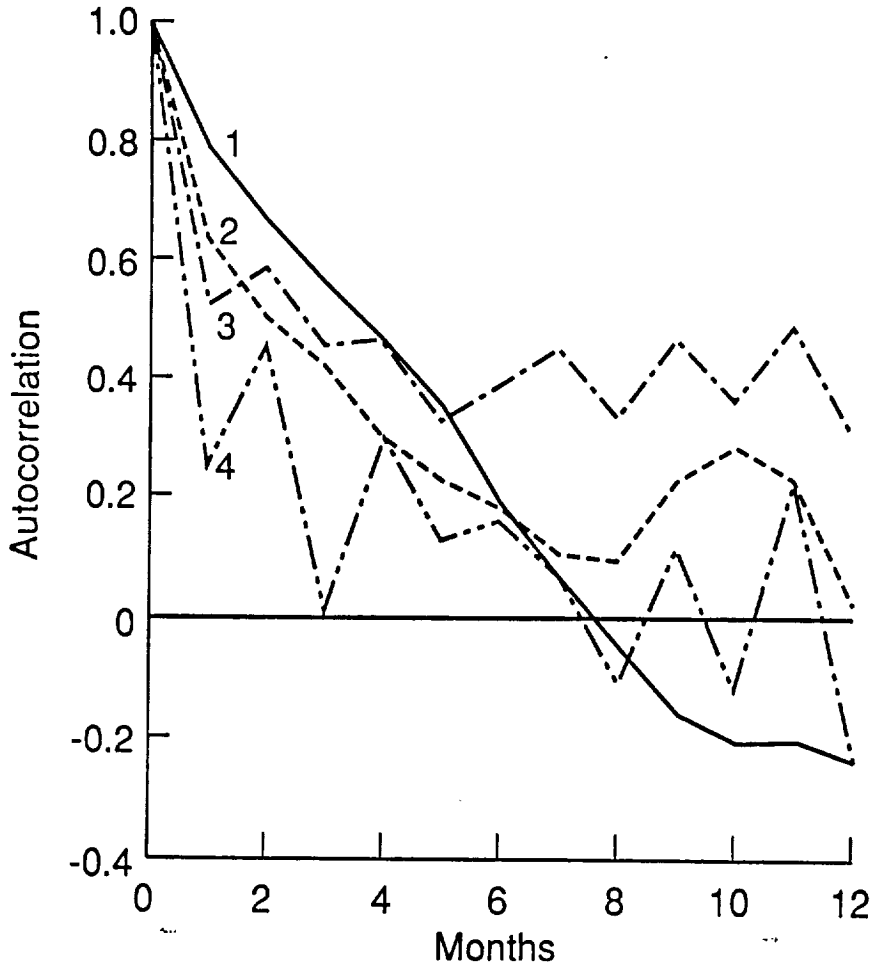

Figure 10. Autocorrelation for EOF's computed with seasonal cycle removed.

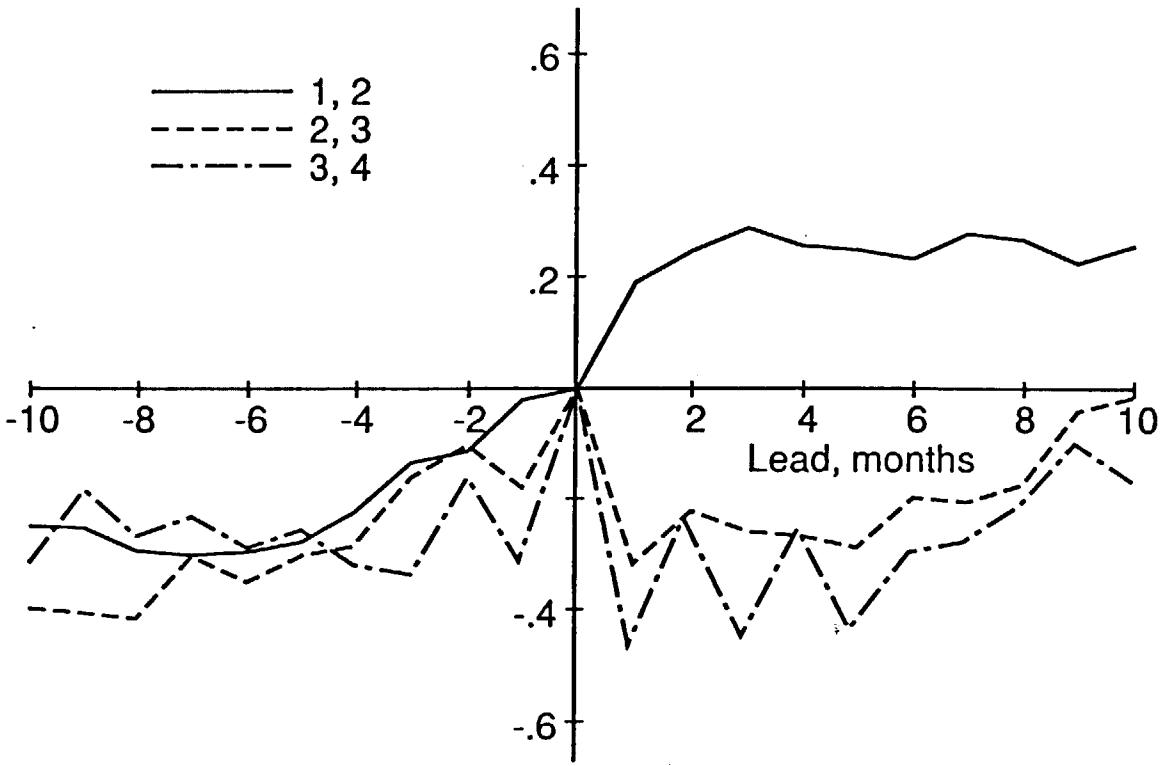

Figure 11. Time-lagged cross correlation coefficents for EOF's computed with seasonal cycle removed.

fig 11